J Mater Sci: Mater Electron (2007) 18:S93–S96
DOI 10.1007/s10854-007-9162-3

Band-edge electroluminescence of crystalline silicon heterostructure solar cells

G. Weiser · S. Kazitsyna-Baranovski · R. Stangl

Published online: 13 March 2007

Abstract Monocrystalline Si solar cells exhibit above 50 K intrinsic electroluminescence which increases with temperature to external efficiencies beyond 0.03%. Spectra derived from the generalized Planck equation suggest that interface recombination is responsible for this temperature dependence. However, these modeled spectra predict too large emission above the gap. Spectra derived from the bandstructure and statistics of electrons, holes and phonons show that even at room temperature light is emitted only by creation of phonons while phonon annihilation does not contribute. The analysis suggests that detailed balance of absorption and emission rates is not achieved for emission at indirect gaps.

1 Introduction

High efficiency Si solar cells show band-edge emission under forward current despite an indirect gap. Devices based on n-type Si wafers reach solar conversion efficiencies beyond 21% [1] and external emission efficiency near 1% [2]. Much simpler devices, heterostructures with a thin n-doped amorphous emitter on p-type wafer show electroluminescence at the bandgap with external power efficiency ranging from 0.013% [3] to more than 0.03% [4] at room temperature. Spectra of such devices are compared with calculated spectra to check the validity of the generalized Planck and Kirchhoff laws [5, 6] for emission at indirect gaps.

G. Weiser (✉) · S. Kazitsyna-Baranovski
Fachbereich Physik, Philipps-Universität Marburg, Renthof 5, 35032 Marburg, Germany
e-mail: weiser@staff.uni-marburg.de

R. Stangl
Abt. Silizium-Photovoltaik, Hahn-Meitner-Institut, Kekuléstr. 5, 12489 Berlin, Germany

2 Experimental procedure and simulation

Heterostructure solar cells of ZnO/a-Si:H(n)/c-Si(p) were prepared standard plasma deposition of a-Si:H from silane onto 1 Ω cm p-type Si wafer [7]. Two types of devices are compared: (A) 8 nm n-a:Si:H emitter layer on a wafer textured by anisotropic etching and a 35 nm a-Si:H(p)/Al backcontact; (B) 20 nm emitter deposited onto a flat interface and Al backcontact. The cells were characterized at 300 K using AM 1.5 illumination (Table 1). The improved absorbance of the textured sample generates larger current and conversion efficiency despite a smaller thickness d of the wafer. However, the sample preparation had no effect on the spectral shape of the intrinsic emission.

Spectra with resolution better than 1 meV were obtained by using a double monochromator, a cooled Ge detector and lock-in technique, modulating either the light emitted by constant current or by using current pulses of low frequency (3–30 Hz). The total emission at room temperature was measured in an integrating sphere. Samples were attached with silver paint to the heat sink of a flow-controlled He cryostat.

Numerical calculations used the program AFORS-HET [8], which simulates observables of heterojunction solar cells from device properties. The simulation employed a standard parameter set [9] for an untextured model structure with 10 nm emitter, an interface with homogeneous

Table 1 Electrical parameter of the solar cells

Sample	J_{SC} (mA/cm^2)	V_{OC} (mV)	FF(%)	η(%)	d (μm)
A	34.1	610	79.9	16.6	220
B	28.9	638	77	14.2	375

distribution of states and 300 μm c-Si(p) wafer. Electroluminescence spectra were calculated by entering absorption spectra of a-Si:H(n) [10] and c-Si [11] while the splitting of the quasi Fermi levels provided the chemical potential in the generalized Planck equation [5].

3 Experimental results

Defect-related emission is observed at low temperature [4, 12] which vanishes with rising temperature to be replaced by intrinsic luminescence with spectra of identical shape, independent of excitation by light or current. Fig. 1 displays spectra of sample B with flat interface taken at decreasing temperatures. The spectrum is dominated by recombination of an electron hole pair with creation of a TO phonon. More fine structure appears at low temperature, attributed to emission of a TA phonon and two-phonon transitions involving Umklapp processes [13]. The peak amplitude increases up to 90 K and the spectrum spreads out towards higher energy. The peak intensity decreases between 100 and 160 K but increases again at higher temperature. This is different from the textured sample A whose peak increased continuously to an almost constant value above 200 K [4]. We observe further that the intensity below 180 K is smaller if the sequence of spectra is taken by starting from low temperature, a hint that electrons and light may not be in thermal equilibrium. The weak emission below 1 eV at low temperature stems from the amorphous emitter pointing to diffusion of holes into that thin layer.

The integrated intensity (inset Fig. 1) increases up to 320 K although the decreasing peak above 90 K leads for sample B to a plateau followed by another increase at higher temperature.

Fig. 2 displays the current dependence of the photon flux and the power efficiency. The light intensity increases linearly with current. Open symbols show the external power efficiency normalized to the consumed power. Despite an higher solar conversion efficiency the textured sample A is a less efficient LED than samples with flat interfaces, B' differing from B only by a thinner emitter layer (5 nm). The power efficiency of B exceeds 0.03% slowly decreasing at high currents due to series resistance. The textured sample A reaches a power efficiency of 0.014% near 80 mA/cm^2 and decreases slowly up to 150 mA/cm^2.

4 Discussion

Detailed balance of photon absorption and emission by excess carriers in a cavity generates a Planck distribution of photons modified only by a chemical potential of photons μ_γ. That equilibrium maintains Kirchhoff's equivalence of absorbance $A(\hbar\omega)$ and emittance resulting in a non-thermal emission similar to thermal radiation [5].

$$J_\gamma = A(\hbar\omega)\frac{(\hbar\omega)^2}{4\pi^2 c^2 \hbar^3}\left[\exp\left(\frac{\hbar\omega - \mu_\gamma}{kT}\right) - 1\right]^{-1} \quad (1)$$

The chemical potential of photons μ_γ is that of electron-hole pairs μ_{eh}, the splitting of the Fermi-levels of electrons and

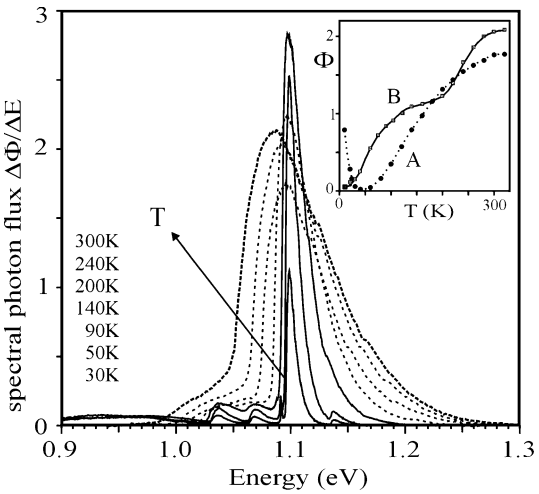

Fig. 1 Electroluminescence spectrum of sample B at different temperatures. The inset shows the integrated intensity of both samples

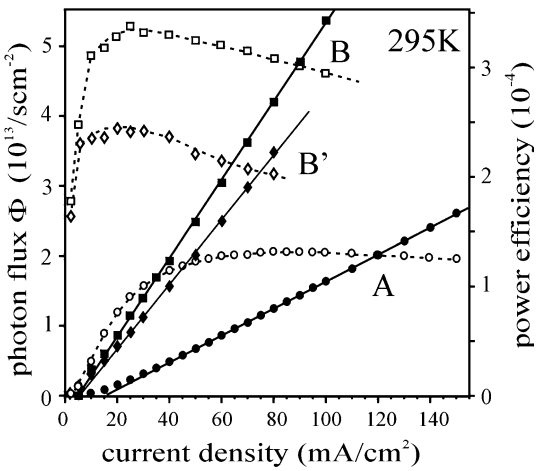

Fig. 2 Integrated intensity (full symbols) and power efficiency (open symbols) of the electroluminescence spectra of samples with flat (B) and textured interface

holes, since emission and absorption of each photon is linked to recombination or generation of one electron-hole pair.

The current J_f of an ideal diode increases exponentially with the forward voltage U_f .

$$J_f = J_s\left[\exp\left(\frac{eU_f}{kT}\right) - 1\right] \tag{2}$$

Minority carrier injection alters the equilibrium density of electrons and holes and the forward voltage defines the chemical potential of excess pairs, $\mu_{eh} = eU_f$. Combining these equations results in the observed linear relation of photon flux and forward current.

$$J_\gamma = A(\hbar\omega)\frac{J_f}{J_s}\frac{(\hbar\omega)^2}{4\pi^2\hbar^3c^2}\exp\left(\frac{-\hbar\omega}{kT}\right) \tag{3}$$

Diffusion of minority carriers defines the saturation current J_s which depends on their concentration at the interface to the neutral region, which is defined by the acceptor concentration N_A and intrinsic carrier concentration n_i [14].

$$J_s = \frac{D_n}{L_n}\frac{n_i^2}{N_A} = \frac{D_n}{L_n}\frac{N_C N_V}{N_A}\exp\left(-\frac{E_g}{kT}\right) \tag{4}$$

The activated saturation current predicts a different temperature dependence of emission of photons with energies smaller or larger than the gap E_g.

$$J_\gamma = A(\hbar\omega)\frac{(\hbar\omega)^2}{4\pi^2\hbar^3c^2}\frac{D_n}{L_n}\frac{N_C N_V}{N_A}\exp\left(\frac{E_g - \hbar\omega}{kT}\right)\cdot J_f \tag{5}$$

Direct semiconductors emit photons with energies larger than E_g and the emission should increase with temperature. Indirect semiconductors emit also photons below the gap by simultaneous emission of a phonon and that efficiency should decrease with increasing temperature.

Fig. 3 presents electroluminescence spectra at various temperatures, derived from Planck's law for 30 mA/cm^2 current and using for all the absorbance at 300 K. Interface densities below 10^{10}/eV cm^2 have negligible influence on the chemical potential μ_{eh} of electron-hole pairs and the temperature dependence of the spectra complies with eq. 5: Emission above the gap increases with temperature while the subgap emission decreases with the crossover marking the gap. Increasing the interface density of states to 10^{11}/eV cm^2 reduces light emission significantly since interface recombination decreases the chemical potential in the neutral region but more striking is the effect on the temperature dependence. Since interface recombination is more efficient at low temperature light emission increases with temperature now throughout the spectrum. We

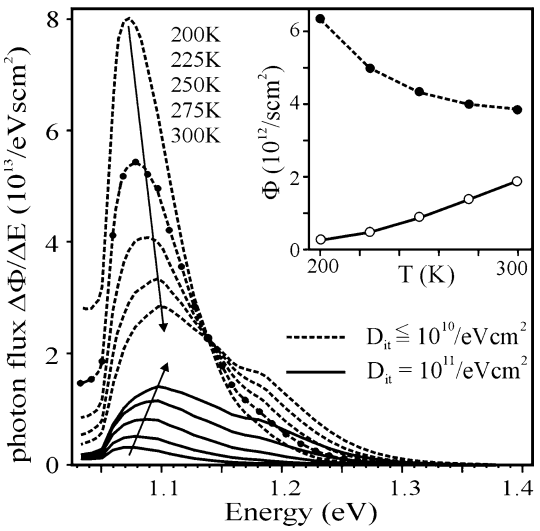

Fig. 3 Simulated emission spectra for different temperature for densities of interface states. The inset shows the total photon flux

conjecture that interface recombination is responsible for the observed increase of light emission with temperature. It is likely that the larger defect density of textured interfaces reduces light emission despite higher solar conversion efficiency.

The simulated spectrum yields a smaller photon flux than measured for sample B and even more surprising reveals significant deviation of its shape from experimental spectrum at high energy (Fig. 4). The shoulder above the gap in the modelled spectrum arises from photons emitted with annihilation of TO phonons but is not found in experimental spectrum.

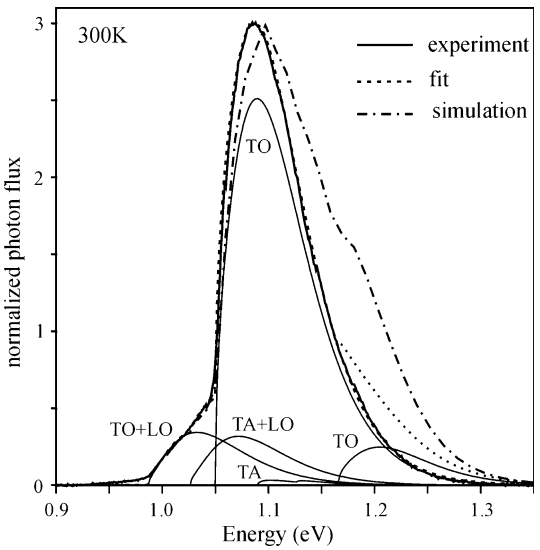

Fig. 4 Comparison of the experimental spectrum with the spectrum derived from the generalized Planck equation. The fit is a spectrum calculated from the density of states and various phonon thresholds

To explore that missing contribution we calculated emission spectra from the density of states, Boltzmann distribution of electrons and holes and proper rates for creation and annihilation of a phonon of energy $\hbar\Omega$.

$$J_\gamma(\hbar\omega) = \mathrm{C} \cdot \left(\hbar\omega - \mathrm{E_g} - \hbar\Omega\right)^{\mathrm{n}} \exp\left(\frac{-\hbar\omega - \hbar\Omega + \mathrm{E_g}}{\mathrm{kT}}\right) \cdot \left(1 + \frac{1}{\exp\frac{\hbar\Omega}{\mathrm{kT}} - 1}\right) \tag{6}$$

The first parenthesis describes the density of states of electron hole pairs where $n = 0.5$ applies to correlated pairs with kinetic energy in their centre of mass motion while $n = 2$ accounts for uncorrelated pairs. The last factor (1 + f) is the probability to create phonons. Spectra at 60 K are exclusively due to correlated pairs [4]. At 300 K these still contribute about 35% and are responsible for the steep onset of the various phonon bands. Most emission comes from recombination of uncorrelated pairs which due to their parabolic density of states (n = 2 in eq. 6) yield spectra without sharp low energy threshold but with more extended high energy tail. The weak lines show the contributions of one- and two-phonon transitions [13]. The TO phonon of 57.8 meV energy contributes 78% to the emission, two-phonon transitions add another 20% while the TA phonon contribution is negligible. The sum of phonon creation processes alone reproduces the experimental spectrum. This result is unexpected since annihilation of the strongly coupling TO phonon should add 10% of the emission. Emission with phonon annihilation has the threshold near 1.16 eV and would create the shoulder shown by the dotted line. This shoulder is weaker than simulated from Planck's equation but nevertheless too strong to fit into the experimental data.

The enhanced emission with phonon annihilation results in the simulation from the strong absorbance A($\hbar\Omega$) in that region. Absorption of photon energies larger than the gap creates a phonon while the reverse process requires annihilation of that phonon. For photon energies less than the gap the opposite condition applies. The ratio (1 + f)/f of phonon creation and annihilation rate favours electron-photon coupling with creation of phonons by the factor $\exp(\hbar\Omega/\mathrm{kT})$. This factor enhances light emission below the gap and suppresses emission in the region of large absorbance. Balance of emission and absorption of light is still achieved if time plays no role as in a cavity, where photons cannot leave and the generalized Planck equation holds [6]. In an open system dynamics is important: Low energy photons escape rather than being reabsorbed while high energy photons generate electron-hole pairs which decay into low energy photons and phonons. Due to the different dynamics of phonon creation and annihilation Kirchhoff's equivalence of absorbance and emittance is not maintained since Planck's equilibrium of low and high energy photons is not achieved. Rapid conversion of high energy phonons into low energy phonons keeps phonons in thermal equilibrium while high energy photons transform effectively into low energy photons via their coupling to electron-hole pairs.

5 Conclusion

Light emission from amorphous-crystalline Si solar cells depends sensitively on the density of interface states and increases linearly with forward current as predicted by the extended Planck equation. Such thermal equilibrium of photons, however, overestimates light emission with simultaneous annihilation of phonons. The absence of noticeable contribution from this process even at 300 K indicates that photons reach not such equilibrium by dynamical reason. Electron-hole pairs interact simultaneously with two different photons and one phonon. Phonon dynamics favours generation of phonons and emission of low energy photons which escape before an equilibrium with high energy photons is established.

References

1. M. Taguchi, H. Sakata, Y. Yoshimine, E. Maruyama, A. Terakawa, and M. Tanaka, Proc. 31st IEE Photovoltaic Specialist Conference 2005, p. 866
2. M.A. Green, J. Zhao, A. Wang, P. J. Reece, M. Gal, Nature **412**, 805 (2001)
3. M.S. Bresler, O.B. Gusev, E.I. Terukov, W. Fuhs, A. Froitzheim, A.S. Gudovskikh, J.P. Kleider, G. Weiser, J. Non-Cryst. Solids **338–340**, 440 (2004)
4. W. Fuhs , A. Laades , K.v. Maydell , R. Stangl, O.B. Gusev, E. I. Terukov, S. Kazitsyna-Baranovski, G. Weiser, to be published. J. non-cryst. solids
5. P. Würfel, J. Phys. C: Solid State Phys. **15**, 3967 (1982)
6. P. Würfel, S. Finkenbeiner, E. Daub, Appl. Phys. **A60**, 67 (1995)
7. K.v. Maydell, E. Conrad, and M. Schmidt, Progress in Photovoltaics (2005), in press
8. R. Stangl, M. Kriegel, M. Schmidt, Proc. Photovoltaic Solar Energy Conf. (PVSEC-20), Barcelona (2005), in press Download www.hmi.de/bereiche/SE/SE1/projects/aSicSi/AFORS-HET.
9. R. Stangl, QA. Froitzheim, M. Schmidt, and W. Fuhs, Proc. 3rd World Conf. on Photovoltaic Energy Conversion (Osaka 2003) 1P-D3–34
10. P. Sladek, M.L. Theye, L. Chahed, J. Non-Cryst. Solids **363**, 164 (1993)
11. M. Green, M. Keevers, Progress Photovoltaic Reports **3**, 189 (1995)
12. P.J. Dean, J.R. Haynes, W.F. Flood, Phys. Rev. **161**, 711 (1967)
13. M. Asche, O.G. Sarbei, phys. stat. sol. (b) **103**, 11 (1981)
14. S.M. Sze, Semiconductor Devices, John Wiley & Sons, New York, 1985 (ISBN 0–471–87424–8)